Journal of The
Electrochemical Society

Microstructure Scale Lithium-Ion Battery Modeling: Part I. On Through-Plane Heterogeneity, Impact of Mesh Representation, and Differences between Macro- and Microscale Models

To cite this article: Francois L. E. Usseglio-Viretta *et al* 2025 *J. Electrochem. Soc.* **172** 080508

View the article online for updates and enhancements.

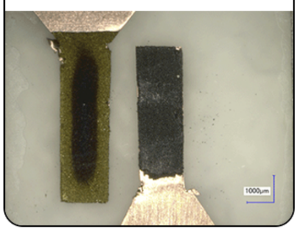

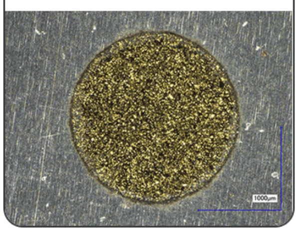

Journal of The Electrochemical Society, 2025 **172** 080508

Microstructure Scale Lithium-Ion Battery Modeling: Part I. On Through-Plane Heterogeneity, Impact of Mesh Representation, and Differences between Macro- and Microscale Models

Francois L. E. Usseglio-Viretta,[1,z] Andrew M. Colclasure,[1] Jeffery Allen,[2] Peter J. Weddle,[1] Donal P. Finegan,[1] Peter Graf,[2] and Kandler Smith[1]

[1]Center for Energy Conversion & Storage Systems, National Renewable Energy Laboratory, Golden, Colorado, 80401, United States of America
[2]Computational Science Center, National Renewable Energy Laboratory, Golden, Colorado, 80401, United States of America

Li-ion battery performance and degradation are strongly correlated with the electrode microstructures and can be modeled at different scales, each with their own limitations. Herein, we compare predictions achieved with a macro- and a micro-scale model, that is, respectively, neglecting or considering the microstructural heterogeneity of the composite electrodes, on virtual numerically generated and real microstructures. While both models are in relative agreement at the low charge rates, differences arise for fast charging scenarios and especially for the real, highly heterogenous, microstructures. The microscale model predicts that electrolyte concentration saturation and depletion, respectively, at the back of the cathode and of the anode are exacerbated, and that lithium plating occurs earlier for real microstructures. The present work also indicates that the mesh representation significantly impacts the microscale model predictions, and consequently that microscale models should add surface area as a parameter to consider explicitly surface roughness. This article is the first of a series, with subsequent entries further investigating in-plane heterogeneities, lithium plating, and the impact of microstructure representativity on model predictions.
 [DOI: 10.1149/1945-7111/adf35d]

Manuscript submitted December 11, 2024; revised manuscript received June 28, 2025. Published August 7, 2025.

Supplementary material for this article is available online

Lithium-ion battery (LIB) electrodes have porous microstructures with the solid matrix being comprised of active material particles, carbon conductive additive and polymer binder additive, and the pore space being filled with an electrolyte solution. LIB performances are strongly correlated with electrode microstructures, as effective transport and kinetic properties are partly determined by the particle morphology and spatial distribution,[1–3] which in-turn influence the achievable capacity.[4,5] Tailoring microstructure parameters has been identified as one possible approach, among others, to enable fast charging in thick electrodes, which are required for automotive applications, without inducing degradation and capacity fade.[5] A key aspect of LIB models is then to accurately capture microstructure influences on rate performance and battery degradation. From this perspective, LIB models can be sorted into three families according to their scale: macro-, meso-, and microscale.

Macroscale models[6–9] use porous electrode theory and abstract microstructural heterogeneity of composite electrodes using effective macroscopic properties, typically porosity ε, specific surface area S_p, particle mean diameter D_{50} and tortuosity factor τ. These models are one-dimensional along the electrode thickness, with an additional dimension along the particle radius and are thus noted as pseudo-2D (P2D). While suitable for design guidance and being fairly successful in matching experimental data,[4,5] these models are intrinsically restricted by their macroscale approach.[10] Numerous limitations exist including: a spherical/isotropic electrode material assumption (inaccurate for certain electrodes with anisotropic effective ionic diffusion such as flake-like graphite[2,3]), assumptions of no in-plane heterogeneity (i.e., the heterogeneity description is limited to the electrode thickness, that is the through-plane direction), restrictions to only capturing the bulk mid-section description (i.e., edge effects and cell form factor impacts are ignored), microstructure description oversimplification (typically, only four parameters are used to represent the complex electrode microstructure and local geometric features such as surface roughness and cracks are not explicitly considered), and microstructure propagation error (microstructure parameter estimation is challenging with an associated error[3,11,12] that propagates to macroscale model predictions). Despite these limitations, macroscale models have proved to be very successful to match experimental data as (i) until recently most experimental measurements are also averaged quantities and are not spatially resolved (e.g., cell voltage is calculated for the whole volume),[4,5] and (ii) microstructure parameters can be fitted to match experimental data points, although at the risk of overfitting. To take into considerations the impacts of microstructural in-plane heterogeneity and spatial variations,[13,14] mesoscale models have been developed for which microstructure parameters can be spatially dependent.[15–18] These models are particularly valuable to investigate electrochemical behavior heterogeneity at different electrode regions, either considering edge effects, distance from the battery tabs, the cell form factor, macroscale pores,[18] and/or microstructural millimeter (or higher) scale heterogeneity.[15–17] However, mesoscale models still rely on microstructure assumptions and effective microstructure parameters, as they essentially add one or two in-plane spatial dimensions to a macroscale P2D model without changing the intrinsic set of equations. Last, microscale models[10,19–32] explicitly solve a system of equations directly on the microstructure geometry (that contains hundreds/thousands of particles), removing both the parameters and assumptions related to the microstructure. That is, instead of extracting parameters used in higher length-scale models from the microstructure (e.g. porosity) and simplifying it description (e.g., particles are spherical), the microstructure geometry itself is the microstructure parameter, which has its own issues as later discussed).

Microscale models are especially relevant to investigate the impact of local features, such as particle cracks or particle surface roughness, on the electrochemical local response as well as predicting the onset and location of local degradation phenomena, such as lithium plating. Indeed, degradation mechanisms *onsets* are driven not by averaged quantities, for which higher scale models excel at determining, but by extremums, i.e., hot spots where concentration and/or potential difference are locally either significantly higher or lower compared with the local through-plane slice-averaged or the cell volume-averaged. Furthermore, extremums are

[z]E-mail: francois.ussegliovirretta@nrel.gov

likely to be even further away from the local slice-average when cycling at relatively high charge and discharge rates, as heterogeneity sinks (bulk diffusivity and conductivity) may not be fast enough to balance the C-rate increasing heterogeneity source (local intercalation reaction at the electrolyte-active material interface). Analyzing the effects of microstructure heterogeneity on battery performance and degradation has practical implications for manufacturers, as it can provide quantitative quality control metrics for microstructure heterogeneity. In-plane heterogeneities and lithium plating analysis are, respectively, the focus of Part II[33] and Part III[34] of this article series.

However, practical considerations limit the use of microscale models, as they typically require 3D imaging capabilities to generate the geometry, and High-Performance Computing (HPC) to solve millions of Degrees of Freedom (DOFs). Conversely, P2D models are widely available to the community. Therefore, in Part I of this article series, we also compare these two model scales, to evaluate the bias and errors induced by the macroscale representation. Furthermore, to determine if microscopic heterogeneities not only induce local variations but also modify the average itself calculated per slice along the cell thickness, predictions between a macro-homogenous and a microstructure scale model can be compared, as the two approaches, respectively, neglect and consider in-plane heterogeneity. However, to be coherent, this comparison requires that both models represent a microstructure without any heterogeneity (e.g., ideal spheres of uniform size randomly distributed), so that differences calculated between the two models, if any, arising with real geometries can be attributed to the microstructure heterogeneity (and/or incorrect macroscale assumptions). Lopata et al.[29] have compared micro- and macroscale models using numerically generated sphere-based microstructures. Their models predicted differences for the through-plane slice-averaged state of lithiation and cell potential despite using this ideal, highly uniform, geometry, with differences increasing with increasing C-rate. Latz et al.[31] also calculated differences in cell voltage and electrolyte salt concentration for sphere-based geometries. The authors showed that for prolate spheroids the calculated concentration profile in the electrolyte deviated even more from the macroscale model, as expected since the spherical assumption was no longer accurate. These two works from Lopata and Latz suggest intrinsic differences between the micro- and macro-scale models subsist despite using spherical particles. It is further discussed in the present work. Higa et al.[19] provided another comparison analysis, albeit with much higher differences, and attributed these differences to using a real microstructure with a small field of view (FOV).

Review of Microstructure-Scale Battery Modeling Analysis

Microstructure scale models have been developed recently due to the combined progress of HPC, required to handle millions of DOFs, and nano-scale imaging, required to describe the morphology of electrode particles and pore channels. Table I summarizes the various models published in the literature, including the one used in this work and initially published in a previous work.[10] Most articles do not model mechanics, damage/degradations (apart from calculating its onset, such as for lithium-plating), and thus confine themselves to a single charge and/or discharge. This is a direct limitation induced by their high CPU-cost. One other simplification made by all the models referenced in this review, except in Lu et al.[26] and Hutzenlaub et al.,[23] consists in neglecting or simplifying the carbon binder domain (CBD), that is homogenizing it or assuming a thin CBD layer at the particle surface. Meshing a heterogenous CBD typically imposes a finer mesh and requires knowing its spatial distribution, the latter being challenging to obtain through X-ray tomography experiments due to the weak X-ray absorbance of this phase. Alternatively, Focused Ion Beam Scanning Electron Microscopy (FIB-SEM), can be used to image the additive domain, albeit at the price of a smaller FOV.[35–37] To overcome this technical limitation, several authors have proposed algorithms to numerically generate the CBD,[38–40] with some open-source software being developed for this task.[41,42] None of the models listed in Table I investigate large volume expansion materials, such as silicon anode, that is the mesh is assumed to be static. In this work, a standard chemistry with homogenized CBD representation and without mechanical modeling is investigated (albeit simulated with a very large FOV, per the standard of battery microstructure scale modeling, cf Table I). The main points of differentiation from the literature are presented in the next section.

Aim and Organization of the Article Series

A LIB electrochemical numerical model has been presented in a previous work,[10] but only with an emphasis on the numerical aspects. The present work focuses on electrochemical performance and degradation and is divided into four parts. The first three articles, Parts I-III investigate electrochemical quantities (e.g., concentration, potential, lithium plating), while the last article, Part IV, evaluates if these results are representative as further explained.

In the present manuscript (Part I), the impact of the electrode microstructure mesh representation used in the microscale model is first discussed, aiming at pointing out that the specific surface area is a parameter that still needs to be defined even with a microscale model. A method to handle surface roughness in a microscale model is also provided. The electrochemical behavior of numerically generated and image-based electrodes for which the electrode geometry does not satisfy completely the assumptions of the macroscale model are compared using a micro- and a macro-scale model. While the microscale models listed in Table I all discuss heterogeneity to some extent, there remains a lack of proper quantification and correlation. This first article quantifies electrode material non-uniform utilization along the cell thickness. The second article, Part II,[33] investigates in-plane heterogeneities with the microscale model (otherwise not available with standard macroscale/P2D modeling) and correlates them with the local material properties and the local microstructure topology. The impact of submicron surface roughness heterogeneity and particle size distributions are also investigated. In the third article, Part III,[34] the preferential lithium plating locations near the anode-separator interface are correlated locally with the microstructure heterogeneity, and lithium plating onset is correlated globally with the effective microstructure parameters, that is answering, respectively, where and when does lithium plating occur? Eventually, our analysis results in design recommendations to reduce heterogeneities proposed at the end of Part III.[34] The model-prediction variability obtained with different sub-volumes is also briefly estimated and leads to Part IV[43] of this article series that focuses on the microstructure representativity analysis.

While microstructure abstraction over-simplification impedes macro- and meso- scale models, microscale models are hindered by the limited FOV that can cause representativity issues. While some articles[20,24,27,28] mentioned Representativity Volume Element (RVE) analysis (cf, Table I), there is, however, a lack of methodology or standardization for the representativity analysis. For instance, no RVE sizes are quantified using the reference methodology described by Kanit et al.,[44] and used in previous works by the authors in Refs. 1, 45. A subvolume extracted from the FOV is not a RVE until a statistical analysis demonstrates it, but rather the subvolume can only be considered as a control volume. Furthermore, RVE analysis requires to characterize *multiple* independent subvolumes (and not a single subvolume as sometimes seen in the literature) to evaluate subvolume representativity. Last, while some control volumes mentioned in these representativity analysis show similar volume fraction or particle size with the full FOV, this is not indicative of the electrochemical behavior representativity. For instance, tortuosity factor, critical to simulating ionic transport at high charge rates, requires a much larger RVE size than volume fractions and particle size.[43,45] Part IV of this article series[43] focuses on the representativity of the microstructure scale analysis, both for

Table I. Summary of microstructure scale LIB models in the literature.

Domain					Physics			Focus of the analysis					Numerical framework			Reference
Domain	FOV[a)]	DOF/number of cell[b)]	CBD representation	Actual (from imaging)/ Generated	Chemistry	Mechanics	Aging mechanism	Representativity	Charge rate[c)]	Micro-macro scale comparison	Lithium plating	Cycling	Generated volume	Meshing	Solver	
Half-cell	15 × 15 × 70 μm^3	/0.2 M	Not considered	Y/N	$LiCoO_2$	None	None	x	8 C	x			n/a	C++ custom code	Not indicated. Finite volume method.	Yan et al.[20]
Full-cell	60 × 60 × 240 μm^3	Not indicated	Not considered	N/Y	Not indicated	None	None		Not indicated	x			Not indicated	Not indicated	BEST	Latz et al.[31]
Full-cell	2D. Not indicated	/13 k	Not considered	N/Y	NMC	None	None		5 C				Not indicated	Not indicated	COMSOL	Meyer et al.[32]
Half- and full-cell	95 × 95 × 695 μm^3	Not indicated (1.9 M voxels)	Thin layer at the active material surface	Y(NMC)/ Y(graphite)	NMC, Graphite	None	None		5 C	x	x		GeoDict	Not indicated	BEST	Danner et al.[21]
Half-cell	48 × 46 × 23 μm^3	/1.5 M	Not considered	Y/N	$LiCoO_2$, NCAO, NMC	None	None		5 C	x			n/a	Mimics	ANSYS Tgrid	Wiedemann et al.[22]
Half-cell	12 × 20 × 26 μm^3	/21 M	Meshed	Y/N	$LiCoO_2$	None	None		1 C				n/a	Pro-STAR	STAR-CCM+	Hutzenlaub et al.[23]
Half-cell	0.75 × 0.75 × 0.75 μm^3	Not indicated	Not considered	Y/N	$LiFePO_4$	None	None	x	4 C				n/a	Simpleware	COMSOL	Kashkooli et al.[24]
Half-cell	6 × 6 × 14 μm^3	Not indicated	Thin layer at the active material surface	Y/N	$LiCoO_2$	Coupled	Swelling		10 C				n/a	Custom code (CDFEM)	SIERRA/Aria	Mendoza et al.[30]
Half-cell	Not indicated	/100 M	Thin layer at the active material surface	Y/N	NMC (single crystal with orientation)	Coupled	Swelling		1 C			x	n/a	Custom code (CDFEM)	SIERRA/Aria	Roberts et al.[25]
Half-cell	43 × 43 × 50 μm^3	/30 M	Meshed	Y/N	NMC	None	None		5 C				n/a	Simpleware	COMSOL	Lu et al.[26]
Half-cell	35 × 35 × 45 μm^3	Not indicated	Homogenized	Y/N	NMC	Coupled	Interfacial debonding	x	5 C			x	n/a	Not indicated	COMSOL	Liu et al.[28]
Half-cell	30 × 30 × 40 μm^3	Not indicated	Homogenized	Y/N	NMC	Coupled	Interfacial debonding	x	5 C				n/a	AVIZO + MeshLab	COMSOL	Xu et al.[27]
Half-cell	11 × 11 × 110 μm^3	Not indicated	Homogenized	Y/N	NMC	None	None		5 C	x			n/a	STAR-CCM+	STAR-CCM+	Higa et al.[19]
Full-cell	64 × 64 × 144 μm^3	-/3.6 M	Not represented	Y/N	Not indicated	None	None		2 C	x	x		MATBOX	ImageJ + BoneJ	STAR-CCM+	Lopata et al.[29]
Full-cell	154 × 144 × 161 μm^3	34 M /-	Homogenized	Y/Y	NMC/graphite	None	None	x [Part IV[43]]	6 C	x	x		MATBOX	MATBOX +ISO2MESH	FENICS	*This work*

a) In-plane length × In-plane length × through-plane (i.e., thickness) length. Thickness includes current collectors only if meshed. b) Maximum number of DOF simulated. c) Maximum discharge/charge rate investigated.

macroscale application (microstructure parameter representativity) and for microscale application (microstructure scale electrochemical response representativity). Part IV aims to provide a detailed methodology for RVE analysis for battery modeling, and eventually indicates if the results from Parts I-III are representative, i.e., predictive, effectively linking both articles.

Microstructure Model and Methods

Full-cell microscale electrochemical modeling.—The electrochemical microscale model used in this work has been extensively described numerically in previous work[10] and is summarized in appendix A4, with key items presented here.

The main simplification of the model lies in its representation of the CBD. CBD characteristic size is orders of magnitude smaller (10–100 nm) than the active material or pore diameters (1–10 μm).[35,37,46] While some microscale models[23,26] explicitly mesh the CBD, with various levels of detail, this procedure requires both a significantly more complex mesh to create and results in a huge increase in DOFs, the latter being poorly compatible with a volume large enough to be representative. Therefore, and as done by other microscale models,[19,27,28] the combined CBD and electrolyte phases are represented as a homogenized medium to maximize the modeled FOV, which is especially valuable for the representativity analysis of Part IV.[43] The impact of CBD on the electrolyte domain is modeled through the use of effective diffusion and conduction coefficients. The impact of the CBD on the solid conductivity is modeled by increasing the active material conductivity, while not directly considering solid conduction within the homogenized {pore +CBD} domain. Since the resulting active material bulk conductivity is much higher than the electrolyte bulk conductivity, at least for a high enough amount of carbon additive, the solid potential heterogeneity is much lower than the electrolyte potential heterogeneity. This implies the heterogeneity of the potential difference at the interface, which is essential to predict the lithium plating onset, is driven by the electrolyte potential heterogeneity in this model. The CBD simplification implies that the active material cluster must be fully connected, that is the particles are fused together. X-ray computed tomography (CT) of both NMC and graphite shows near full active material connectivity,[3] which supports this assumption. However, FIB-SEM imaging with the CBD phase resolved indicates that NMC particles are rarely in direct contact, but are typically connected through the CBD.[37] For the numerically generated microstructures later introduced in the manuscript, the connected condition is enforced by allowing moderate overlapping between the active material particles.

Solid transport is assumed isotropic (neglecting NMC crystallographic grain structure, otherwise investigated in previous works at the particle-scale[47,48]) and without phase change (neglecting graphite phase or stage transition, otherwise investigated in previous work experimentally[14]). Temperature is considered constant and uniform in this work, with materials coefficients defined for 30°C, and listed in appendix A5.

The actual surface area cannot be determined from nanoscale imaging, due to its apparent fractal nature (surface area is highly sensitive with image resolution, and may not converge, as seen in previous work,[2] Fig. 18). The fractal property of energy material microstructures has been investigated by Bertei et al.[49] Similarly, the meshed active interface area does not reflect the actual interface area, as it is deduced from the same 3D array. The interfacial reaction flux term in the integral of Table A4-II can be modified in the microscale model to correct the mesh surface area, to match an experimentally determined surface area value (e.g., from BET measurement): $\iint_{\mathrm{I}_{me}} j_{me}(S_{r,m}dS)$ instead of $\iint_{\mathrm{I}_{me}} j_{me}dS$, with j_{me} the Faraday current density of electrode m ($m = a$ for anode and $m = c$ for cathode), I_{me} the interface domain between the electrode m and the electrolyte, and dS the surface element. The coefficient $S_{r,m}$ corresponds then to a surface roughness correction term. It is applied on the Faraday current density term (i.e., $\iint_{\mathrm{I}_{me}} (j_{me}S_{r,m})dS$, which is equivalent), but its physical interpretation is a modified surface, that in turn modifies the current density and the associated potentials. Such correction is only to be applied for surfaces within the FOV (intercalation reaction), and not at the edges (applied loading) for which surfaces are plane without roughness. For ideal geometries (i.e., no surface roughness), cuboid meshes induce a surface overestimation that must be corrected.[50] For instance, voxelized spheres of radius r have a numerical surface area of $6\pi r^2$ instead of the actual $4\pi r^2$, thus $S_{r,m} = 2/3$ for spheres. Note that this surface overestimation is not due to an insufficient image resolution, but is intrinsic to the voxelized discretization.[50] That is, there are two sources of error for the calculation of the specific surface area for voxelized ideal spheres: (i) insufficient image resolution and (ii) the voxel discretization itself. While the first error can be removed by simply increasing the image resolution (i.e., voxel length « sphere diameter), the second is intrinsic with the representation of a sphere with tiny cubes. The corrective factor $S_{r,m}$ takes care of this second source of error. For real geometries with surface roughness not depicted by the mesh, $S_{r,m}$ should be >1. In this work, if not indicated otherwise $S_{r,a} = S_{r,c} = 1$.

Only the constant-current (CC) part of a typical constant-current—constant-voltage (CC-CV) charge profile is considered in this work to reduce HPC time. The CV-part is less relevant for this work as we focus on heterogeneity, which shrinks partly during the CV-part due to the lower C-rate. Additionally, lithium plating usually occurs during the CC part portion of fast charging. Once the cell voltage $\langle\phi_{s,c}\rangle_{\Gamma_c} - \langle\phi_{s,a}\rangle_{\Gamma_a}$ reaches the cut-off voltage (4.2 V in this work), the simulation is stopped. The solid potential is noted as $\phi_{s,m}$ with $m = a$ for anode and $m = c$ for cathode, $\langle A\rangle_B$ is the averaged quantity of A over domain B (if B is not indicated, then it is the volume-average of A). The domain Γ_m is the solid interface with the current collector (cf Fig. A4-1). As defined, the *theoretical* C-rate C_{th} determines the current required to transport *all* the lithium moles from the cathode to the anode in $1/C_{th}$ hour(s) (cf Table A4-II, "applied loading" row). From this point on, the term C-rate refers to the *practical* C-rate, i.e., $SOC_{range,c} \times C_{th}$, with a state of charge (SOC) range equals to 0.6 for the cathode material investigated in this work (NMC 532).

The model is initialized using a uniform potential and concentration in each domain. Concentrations are set to $C_e = 1200$ mol.m^{-3}, $C_{s,a} = 1400$ mol.m^{-3} (0.05 SOC), and $C_{s,c} = 44640$ mol.m^{-3} (i.e., 0.90 SOC), respectively for the electrolyte, the anode active material, and the cathode active material, if not specified otherwise. The potential initialization is realized sequentially as explained in appendix A4.

The model mesh sensitivity and time step sensitivity analysis with the mass conservation error are available, respectively, in appendix A7 and A8.

Micro-macro scale model comparison methodology.—The microscale model is first compared with a well-established macroscale homogeneous model[51] based upon the P2D formulation originally proposed by Newman and coworkers[6] that has been validated with experimental data in previous works.[4,5] Two conditions are required to achieve an expected match between the two models: (i) using a microstructure that satisfies the microstructure assumptions of the macroscale model, i.e., non-overlapping ideal spherical particles randomly distributed, and (ii) using microstructure parameters that match the electrode geometry FOV (this second condition is further detailed in the *electrode library and material coefficients* section). Note that achieving FOV representativity is not a requirement for the comparison analysis, as long as the microstructure geometry and the microstructure parameters match the condition that microstructure is highly uniform. Since actual LIB electrodes do not perfectly match the macroscale model assumptions, virtual microstructures can be tailored to specifically reach these conditions for the comparison analysis. A microstructure generation algorithm is presented in appendix A1. The microstructure generation algorithm is also used to generate microstructures that differently satisfy the isotropy and morphology assumptions of the macroscale model (i.e., non-spherical particles with various alignments). This allows to quantify the errors induced by using no longer correct assumptions in the macroscale model. The as-generated microstructures are detailed in the *electrode library and material coefficients* section. The two models are then used on actual X-ray CT microstructures that do not match necessarily macroscale microstructure assumptions (using a macroscale model on a microstructure means extracting its effective parameters, while using a microscale model on a microstructure means using its 3D geometry as a mesh). Here, differences between the models would be primarily attributed to the over simplified representation of the microstructure used in the macroscale model.

Near uniform potentials and concentrations occur during very low charge rates as the heterogeneity source (intercalation reaction flux) is largely overcome by the heterogeneity sinks (bulk diffusivity and conductivity). In such a case, macroscale model predictions are nearly independent from microstructure parameters, except for the porosity, as there are no kinetic or transport limitations. For instance, the macroscale Single Particle Model (SPM) neglects electrolyte gradients all together (no tortuosity microstructure parameter), and therefore is only relevant when cycling at very low C-rates.[52] This implies that error propagation, from the microstructure representation (either from incorrect parameters or incorrect morphology assumptions) to the electrochemical response predicted with a macroscale model, is expected to increase with the increasing C-rate. In other words, a more accurate representation and characterization of the microstructure is required for fast-charge modeling.[12] The more refined the microstructure description is (e.g., upscaling from the SPM to the P2D model), the lower the error will increase with an increasing C-rate. Therefore, different C-rates are considered for the present comparison analysis.

Microstructure generation and meshing.—Virtual microstructures are numerically generated to compare micro- and macro- scale models, with method detailed in appendix A1.

The meshing of the complex tortuous LIB electrode microstructure is a challenging task that can hinder microscale modeling. In this work, microstructure geometries are first pre-processed with two steps detailed in appendix A2: (i) a standard erosion-dilation step (i.e., morphology opening) to reduce surface roughness and ease the meshing process, and (ii) an original phase and voxel connectivity correction step to ensure full connectivity of the phases (required for the micromodel) and to correct ill-defined voxel connections that can otherwise fail the meshing process and result in singular flux vertices detrimental to the model numerical stability.

The meshing itself is detailed in appendix A3 and is performed using either a regular structured or an unstructured grid to investigate the impact of the mesh representation on the electrochemical response, notably by changing the active surface area. The regular structured meshes keep the cuboid representation while the unstructured meshes provide a smoother interface. The meshing uses a third-party open-source software Iso2mesh for the unstructured meshing generation.[53,54]

Both microstructure generation, preprocessing, and meshing are accomplished using the open-source NREL Microstructure Analysis Toolbox (MATBOX).[41,42] MATBOX provides algorithms for microstructure segmentation, numerical generation, characterization, homogenization, and meshing, embedded in a user-friendly graphic-user interface.

Electrode Library and Material Coefficients

All material coefficients are available in the supplementary materials and are plotted in Fig. A5-1 and listed in Table A5-I, while electrode microstructure parameters are listed in Table A6-I.

Numerically generated volumes.— *Full cell microstructures for micro-macroscale comparison analysis.*—Generated microstructure volumes have a FOV of $100 \times 100\ \mu m^2$ with a thickness of $70\ \mu m$. The cathode has a $\approx$50%vol active material and the anodes have a $\approx$60%vol active material. The N/P ratio, as defined as the practical capacity ratio between the anode and the cathode, is $\approx$1.145. A single cathode volume is generated and consists of slightly overlapping, randomly distributed, spherical particles. Four anode volumes are generated: spherical particles (case *s*), oblate spheroids (i.e., ellipsoids with two identical long diameters, and a third lower diameter) with random alignment (case *r*), aligned oblate spheroids (case *a*), and misaligned oblate spheroids (case *m*). The oblate spheroid particle morphology was selected as it is the typical particle shape of LIB electrode materials from the analysis of 19 electrodes realized in previous work, especially for graphite.[2] The aligned (resp. misaligned) case corresponds to the short diameter being set perpendicular (resp. parallel) with the electrode thickness, with a $+/-15°$ orientation variation from the imposed alignment. All particles share the same size, with a volume-equivalent diameter ($2\sqrt[3]{3V/4\pi}$ with V the particle volume) of $\approx 10\ \mu m$, and an aspect ratio of 3:3:1 for the oblates (that is long diameter is 3 times longer than the small diameter). Particle voxelization is realized with 21 voxels along the sphere diameter, 30 voxels along the oblate long diameters, and 10 voxels along the oblate short diameter, with a voxel size of $0.481\ \mu m$. Diameters used for the macroscale model calculation are determined from the image (i.e., recalculated) to have the real value. This means that instead of assuming what the particle diameter is, we re-calculate it from the generated images. Since particles are overlapping, their shapes are slightly modified: they are not anymore independent spheres or ellipsoids, and so their "diameter" is not as simply defined compared to independent particles. All graphite cases share the same volume fractions and particle volume (but not necessarily the same mean effective diameter as explained in the *Coefficients* subsection). Specific surface area and tortuosity factor are different. Figure 2 shows the microstructure geometries.

Case *s* is the reference geometry for which it is expected that the two models will have the best agreement among the four investigated cases, as it corresponds closely to the macroscale model microstructure assumptions (except for the particles overlapping). Case *r* partially matches the macroscale model assumptions: the effective ionic transport is isotropic due to the particle random alignment which results in no preferential direction at the macroscale, but the particles are no longer spherical (i.e., global isotropy but local anisotropy). Cases *a* and *m* do not satisfy both global and local isotropy (effective transport is anisotropic and particles are not spherical).

Electrodes are meshed with an unstructured grid that provides a smooth active interface. Case *s* is also meshed with a structured grid which retains the cuboid-voxel representation. Figure A3-1 illustrates the structured and unstructured grids. Here, the objective is to quantify the impact of the mesh surface representation by changing the surface area. Last, Case *s* is also simulated with a structured mesh and a corrective factor $S_{r,a} = S_{r,c} = 2/3$ to determine if a simpler, albeit DOF-expensive, cuboid mesh can predict a similar cell voltage with a more complex, but DOF-cheaper, unstructured mesh through a simple surface correction parameter. This approach is similar to the surface area overestimation correction used for nanoscale imaging microstructure characterization.[1,50,55,56] While the smooth surface representation is indubitably better for these well-defined geometries with ideal surfaces, actual electrode microstructures have an unknown surface roughness. Surface smoothing, while visually appealing, is likely to underestimate the real active surface area, and from this point of view, the cuboid representation is likely closer to the real surface area (from a macroscale perspective) as compared to the smooth-surface representation. For electrochemical simulations that do not consider mechanics, in which such sharp angles may introduce artifacts (irrelevant stress concentration), a cuboid representation is still reasonable, therefore trading a (significantly) higher wall-clock time for a very simple and robust mesh generation may be worthwhile.

Tomography-based volumes.—Nickel Manganese Cobalt Oxide $Li(Ni_{0.5}Mn_{0.3}Co_{0.2})O_2$ cathode (NMC532, TODA America Inc.), CGP-A12 graphite anode (ConocoPhillips Inc.), and SLC1506T2 (Superior Graphite) imaged with X-ray Computed tomography (CT) from a previous work[3] are utilized. The weight ratio, active material/carbon black/binder, is 90/5/5 (NMC/C45/PVDF) for the cathode, and 92/2/6 (SLC or A12/C45/PVDF) for the anodes (C45: Timcal carbon, PVDF: polyvinylidene fluoride, Solvay Solef 5130 in the cathode and Kureha 9300 in the anode). Combined with density information, the additive phase is deduced to be 21.97%vol and 9.49%vol of the total solid phase volume, respectively, for the cathode and the anode, which is used to calculate the expected additive phase volume fraction from X-ray CT imaging. To enable full-cell meshing, electrode volumes from the same cell were scaled and cropped so that both volumes (anode and cathode) share, respectively, the same voxel size and the same in-plane FOV. A finer image resolution has been used for the A12 graphite as it exhibits smaller geometric features (e.g., cracks) and particle diameters (cf Table A6-I) than SLC graphite. As a consequence, a smaller FOV was achieved for A12 graphite. The in-plane FOVs and voxel size for the NMC532-A12 cell (labelled as Round 1) and the NMC532-SLC1506T2 (labelled as Round 2) are $43.0 \times 43.0\ \mu m^2$, 260 nm and $144.4 \times 154.4\ \mu m^2$, 600 nm, respectively. Because of the small in-plane FOV available for the Round 1 cell, which is likely to be not representative of the whole electrode volume, analysis for this cell is focused only on its local electrochemical response (i.e., no macroscale metrics are investigated for round 1). The Round 2 cell benefits from a relatively large in-plane FOV and is thus more suited for macroscale predictions (e.g., cell voltage) and heterogeneity analysis. The Round 2 cell model prediction representativity is then investigated in Part IV.[43] Performance metrics between these two cells are not compared directly due to their difference in microstructure representativeness and image resolution, which would bias the comparison. Cell thicknesses (anode, separator, and cathode) are $74.2 + 20 + 71.3\ \mu m$ and $69.7 + 20 + 71.2\ \mu m$, respectively for Round 1 and Round 2. The cathodes have a ≈49.2%vol and ≈49.2%vol active material, the anodes have ≈55.4%vol and ≈57.9%vol active material for Round 1 and Round 2, respectively. The N/P ratios are ≈1.064 and ≈1.121 for Round 1 and 2, respectively. Figures 5 and 6 show the electrode volumes.

Microstructure parameters for macroscale model.—Table A6-I documents the macroscale model properties used for the comparison of the microscale model and macroscale model simulations. The macromodel necessarily requires parameters that describe the underlying microstructure. Microstructure characterization is method-dependent for specific surface area,[1,50,56] tortuosity factor,[3] and particle size.[2] Therefore, to provide a relevant comparison between a microstructure scale and a macroscale model, the homogenized microstructure parameters must be calculated carefully. The methods used to extract these homogenized parameters are detailed in appendix A6.

Electrochemical coefficients for micro- and macro- scale models.—Electrochemical coefficients are listed in Table A5-I and are plotted in Fig. A5-1. The electrolyte diffusion, conductivity, activity, and transference number are concentration dependent. Some of the material coefficient expressions from the literature were re-fit to avoid non-physical values (e.g., negative transport coefficient) outside of the range for which these expressions were initially measured or fitted, typically for low (cf Figs. A5-1b, c) or high concentrations (cf Figs. A5-1d, e, h). Outside the range of measurements, coefficients were assigned to constant values (e.g., high diffusivity at low concentration, cf Fig. A5c) or their expression were continued to an expected value (e.g., exchange current density i_0 should converge to zero at low concentration, cf Fig. A5b). Such extreme concentrations are more likely to occur in a microscale model as compared to a macroscale model due to the local extremums, therefore concentration-dependent coefficient expressions need to be valid over a wider concentration range to avoid numerical error. Additionally, the anode Open Circuit Potential (OCP) expression E had to be rewritten in a different, albeit equivalent, mathematical form to enable numerical convergence in the FEniCS solver. A polynomial piecewise expression E' (cf eq. A5-1, $E' \approx E$) has been selected for this task, with details available in appendix A5.

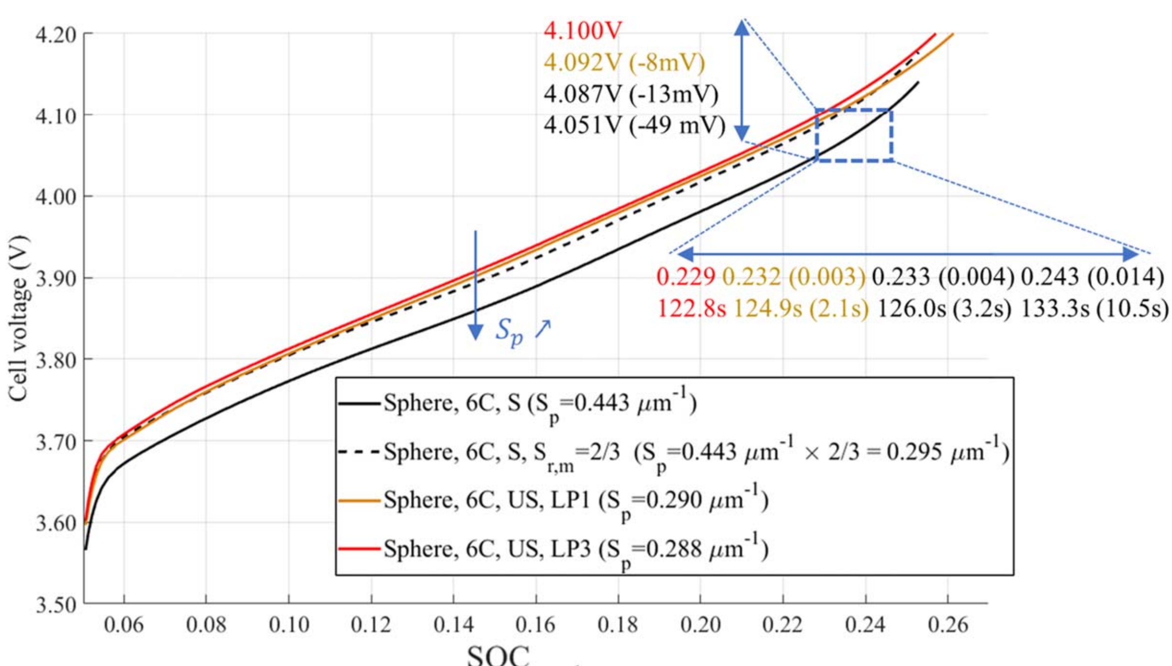

Figure 1. Cell voltage calculated on numerically generated sphere-based full cell (case *s*) at 6 C using different mesh representation. Top right numbers indicate the cell voltage, SOC_{anode}, and time calculated for each mesh, with numbers in bracket being the difference with the US LP3 mesh.

Results

Impact of the mesh representation.—Figure 1 shows the cell voltage calculated using the microstructure scale model for a numerically generated full cell with spherical particles (case *s*) during a 6 C charge. The four different mesh representations are compared:

- "S": structured (i.e., cuboid voxel representation) without a surface roughness correction term (i.e., $S_{r,m} = 1$, cf Table A4-II).
- "S, $S_{r,m} = 2/3$": structured with a surface roughness correction term $S_{r,m}$ equals to 2/3, that is, to correct for the surface overestimation induced by the voxel representation.[50]
- "US, LP1": unstructured with a single smoothing iteration using the lowpass method (cf appendix A3).
- "US, LP3": unstructured with three smoothing iterations using the lowpass method.

Figures A3-1 and A7-2 illustrate the visual difference between structured and unstructured meshes. The difference between different levels of smoothing (US, LP1 vs US, LP3) is negligible. The model predicts that the structured mesh without the surface roughness correction provides a significantly lower cell voltage as compared to the smoothed mesh. The difference at 6 C in the 4.1 V vicinity is 49 mV, with 1.4% SOC or 10.5 s required to match the cell voltage calculated with the unstructured mesh. With the surface roughness correction term applied, the structured and unstructured meshes predict much more similar cell voltage (13 mV difference at 4.1 V vicinity). A refined level of smoothness induces minor variations of the cell voltage, ≈8 mV. For all four cases, the cell voltage variation can be explained by the difference in specific surface area (cf, Fig. 1). Unlike the potential, the impact of mesh representation on concentration is minimal, with a ≈20 $mol.m^{-3}$ maximum difference calculated on the electrolyte concentration (if plotted, all four concentration profiles along the thickness overlap visually). This is expected as the choice of the mesh representation only modifies edges, while the bulk volume is nearly unchanged. For ideal geometries without surface roughness, the smoothest mesh (US LP3) can be considered the closest approximation to the ground truth. However, for real materials with surface roughness, the visually appealing, smooth mesh may be the less representative from a macroscale perspective as it underestimates the true surface area even more than a cuboid representation.

This result demonstrates that potential-related metrics predicted with a microstructure scale model, calculated on the same overall geometry (i.e., no difference in the bulk volume) but with different surface roughness can predict similar cell or electrode scale metrics (e.g., cell voltage) by introducing a surface correction term, which is equivalent to applying a correction on the exchange current density. These results go beyond a simple mesh sensitivity analysis but change the way to use, in practice, microstructure scale models. Indeed, the surface area determined from a microstructure scale image-based analysis is biased by the unknown true surface roughness, as more features become visible with finer image resolution until a cut-off resolution is reached, beyond which the roughness disappears, that is, the fractal behavior eventually collapses.[49] This results in a systematic underestimation of the true specific surface area as seen in a previous work,[2] that, unlike for volumetric metrics such as tortuosity, we cannot extrapolate due to the inherent fractal nature of the surface. Using the surface area provided by the mesh without modification implies assuming that the surface roughness is completely described at the mesh resolution used, which is incorrect for real materials with the current X-ray CT image resolution capabilities with large FOV. Potentials calculated with microstructure scale models are very sensitive with the choice of the mesh representation, with highly smoothed meshes artificially increasing the cell overpotential.

In this article series, as we focus primarily on heterogeneity (Parts II-III[33,34]) and on representativity (Part IV[43]), the absolute potential values are of lower interest. We therefore chose not to modify the mesh surface (i.e., $S_{r,m} = 1$ if not specified otherwise). When absolute values are the primary focus, such as for the micro-macro model comparison analysis, both models are run with the same specific surface area. However, if the analysis were instead intended to be predictive of experimental data, a fitting step of $S_{r,m}$ would be required. If not specified otherwise, subsequent results use unstructured meshes with one smoothing iteration with the lowpass method (i.e., US LP1). Mesh sensitivity analysis for mass conservation error as a function of voxel size and mesh representation (structured and unstructured) is available in appendix A6.

Microstructure/macroscale model comparison.—The microscale model predictions are compared with a macroscale P2D model, first on numerically generated volumes with geometries that satisfy differently the macroscale assumptions (i.e., overlapping spheres are closer to the macroscale representation than overlapping ellipsoids), and then on round 2 actual geometries.

On numerically generated geometries with different particle morphology.—Figure 2 shows the anode concentration with the 4 different anode particle morphologies. As expected, the particle morphology plays an important role on the material utilization, with aligned and misaligned ellipsoids being, respectively, the best and the worst cases, in agreement with their respective tortuosity factor (cf Table A6-I). Sphere and randomly aligned ellipsoids appear to have similar polarization responses.

Figure 3a shows the simulated cell voltage for the 4 different graphites using both microscale and macroscale models. The microscale model systematically predicts lower polarization for all geometries, with ≈−30 mV maximum difference at 1 C for spheres,

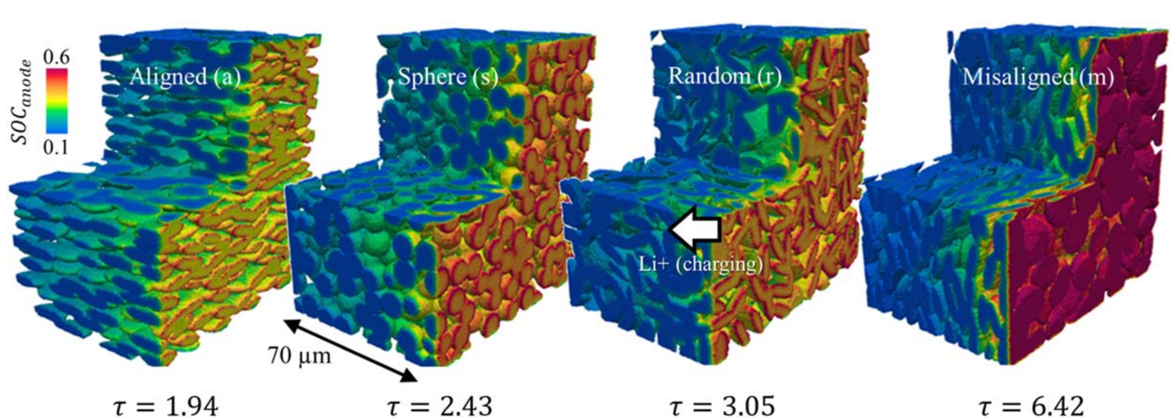

Figure 2. Solid concentration snapshot at 60 s for a 6 C charge for the 4 graphite geometries. CC and separator (not visible) are located on the left and right side of each electrode, respectively. Anode tortuosity along the thickness is indicated below each microstructure. The simulated cathode volume is not shown.

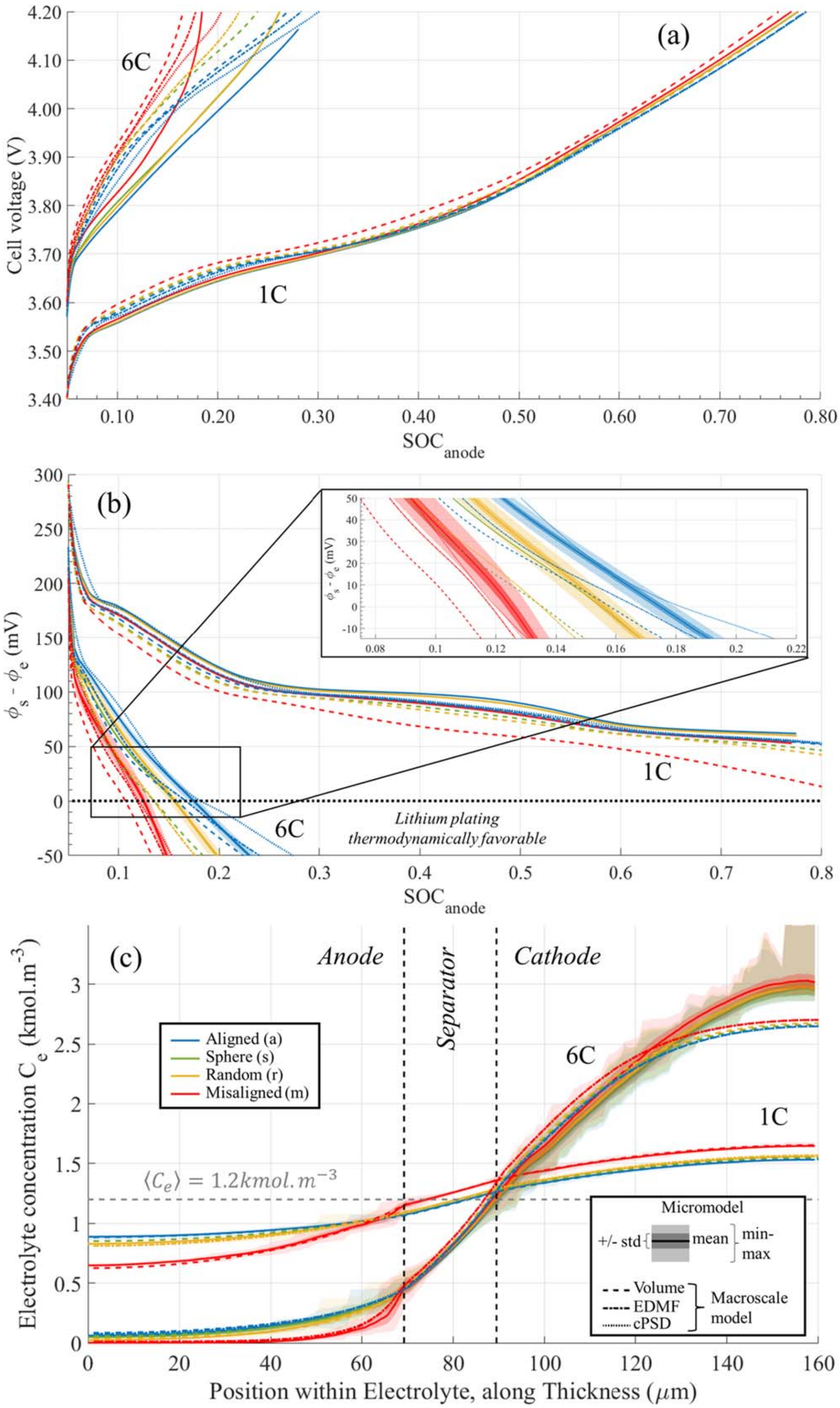

Figure 3. (a) Cell voltage, (b) potential for lithium plating, (c) electrolyte concentration through-plane profile at $\langle SOC_{anode} \rangle = 0.15$ calculated for the numerically generated microstructures with the macroscale model (dashed lines) and the microstructure scale model (solid lines).

and with difference increasing with increasing C-rate. The cell voltage is also very sensitive with the particle size used in the macroscale model, with smaller particle size (cPSD method, cf A6) reducing the difference between the two models (≈ -10 mV at 1 C). A similar trend has been calculated by Lopata[29] (≈ -10 mV at 1 C), using a similar, albeit thinner, sphere-based geometry generated also with MATBOX, as done in this work. Latz[31] also predicted a difference in cell voltage between a homogenized model and a microscale model for a sphere-based geometry. Although, unlike the present and Lopata works, Latz predicted a higher cell voltage for the microscale model. As seen in Fig. 1, the mesh representation can explain the difference in cell voltage. However, Lopata provided the macroscale model with the surface area computed from the 3D smoothed geometry, as done in the present work, to avoid such issue.

Figure 3b shows the potential for lithium plating. For spherical particles, the macromodel predicts earlier plating at 6 C (≈20 mV difference). For ellipsoids, the macroscale model predicts that the 10 μm volume-based diameter produces significantly different responses as compared to the microscale model. However, it should be considered that the solid-state diffusion distance (the characteristic distance used as "radius" in a P2D model) is much smaller in the microscale model as compared to the volume-based diameter used in the P2D model for ellipsoids. These curves demonstrate the consequences of selecting a non-relevant method for the diameter estimation. The two other, more relevant, diameters instead provide smaller differences. The macromodel reaches the plating condition ≈10 mV ahead of the micromodel (and < 2 mV from the micromodel minimum) for the misaligned case, and ≈5 mV before or after the micromodel depending on the selected diameter for the aligned case at 6 C.

Figure 3c shows the electrolyte concentration profile along the cell thickness at 1 and 6 C at $\langle SOC_{anode} \rangle = 0.15$, that is once the profile is roughly steady. Similar predictions between the two models are achieved at 1 C, with a slightly higher slope for the macromodel. At 6 C, the micromodel predicts slightly more electrolyte depletion in the anode, and a significantly higher electrolyte concentration ($\approx +330$ mol m^{-3}) at the back of the cathode, near the current collector, for all geometries. These differences can be explained by the poor electrolyte diffusivity realized at high concentration (cf Fig. A5-1d). Indeed, a local diffusivity that is not high enough to homogenize the local concentration results in a locally high heterogeneity (as seen in Fig. 3c, see significant in-plane standard deviation). Regions with higher electrolyte concentration (due to local microstructure topology) will negatively affect the adjacent regions due to in-series and in-parallel (transversal) interactions. This will shift the average concentration toward higher values. Additionally, since mass is conserved, these relatively higher salt concentrations in the cathode result in lower concentrations far from the positive current collector in the micromodel (cf, Fig. 3c). The authors suspect that the electrolyte profile concentrations are more accurately predicted at fast charge rate with the micromodel due to the inability for the macromodel to handle the detrimental consequences of significant concentration differences due to in-plane heterogeneity.

Since the micro- and macroscale models do not match perfectly for the sphere geometry, intrinsic differences remain between the two models, and/or the assumptions still do not match even for the sphere-geometry tested. This is further elaborated in the discussion section. Therefore, it is still difficult to quantify the contribution of heterogeneity alone on the predicted slice-per-slice average for real, highly heterogenous microstructures.

On tomography-based graphite-NMC geometries.—Only the diameters calculated with the continuum particle size distribution (c-PSD, cf appendix A6) method (that is the smaller diameter) are used in the macroscale model as the other diameter metrics resulted in even larger differences when comparing the two model predictions. While the overpotential calculated for the ideal geometries was systematically larger with the macroscale model, here the cell voltage calculated when using a given model is sometimes higher or lower than the value calculated with the other model (cf, Fig. 4a). A significant difference is realized for the lithium plating potential when charging at 6 C: here the micromodel is more conservative with a plating onset predicted at ≈0.15 SOC_{anode} as compared to ≈0.22 SOC_{anode} for the macroscale model. However, at 4 C both models predict the same onset (albeit with a different trajectory), and at 1 C the macroscale model is more conservative, which prevents making a general conclusion about the relative conservativeness of the microscale and macroscale models. Overall, the micromodel seems to reproduce much more features of the anode OCP profile as compared to the macroscale model prediction (which is especially visible at 1 C). For the electrolyte concentration profile, the very same remarks formulated for the ideal geometries still stand, especially a significantly higher concentration is predicted near the positive current collector with the microscale model, which in consequence aggravates electrolyte depletion at the back of the anode. It answers the question: "does heterogeneity not only induce variations around an average but does it also modify the average itself." It appears the answer is yes for the electrolyte concentration profile, albeit only at fast charge and near the back of the cathode where Li-ion diffusivity becomes very poor.

Electrode material through-plane non-uniform utilization.—Figure 5 shows the concentration fields calculated within the image-based volumes of Round 2 (top) and Round 1 (bottom) during a 6 C charge. While both cathodes have nearly spherical particles, the graphite morphology is significantly different between the two anodes. Particle elongation is much more pronounced for A12 (Round 1) as compared to SLC1506T2 (Round 2) graphite. For both cases, longer diameters are realized perpendicular to the cell thickness as quantified in previous work.[2] In both cells, the through-plane lithiation heterogeneity is significant in the anode and the electrolyte with, respectively, material overutilization near the separator interface, and electrolyte depletion at the back of the anode. Conversely, the cathodes exhibit a flatter average profile along the thickness. However, higher in-plane heterogeneity is calculated for the cathode. Indeed, within-particle concentration homogenization is much faster for the graphite than the NMC due to higher solid-state diffusion (cf Table A5-I and Fig. A5-1) and lower distance-based effective diameters (Euclidean distance map fitting EDMF or c-PSD methods, cf Table A6-I) in the graphite. The A12 graphite has a variety of particle shapes and sizes within a relatively small FOV, with larger particles having slower lithiation dynamics as compared to smaller particles. The model predicts higher intercalation current densities for the large particle near the separator as compared to nearby smaller active materials (cf, Fig. 6). This suggests the existence of a balancing mechanism aiming to reduce, or at least constrain, lithiation difference between nearby particles of different size, in agreement with the model results from Meyer et al.[32] The higher image resolution of the Round 1 cell provides more surface detail for both electrodes. In particular, the model predicts relatively high variations of intercalation current density at the NMC particle surfaces. It is, however, difficult to conclude on both observations (the impact of size distribution and the impact of surface roughness) as (i) the FOV is quite limited for Round 1 Cell and (ii) all features are present, to various extent, within real microstructures, implying that deconvoluting their respective impact is challenging. To remedy these issues, these local, in-plane, heterogeneity are later investigated in Part II[33] using numerically generated microstructures to study them independently.

Figure 7 shows the concentration and intercalation (or Faraday) current density (defined in Table A4-II) profiles along the cell thickness for the Round 2 cell during a 6 C charge. The model predicts that the anode material is saturating at the separator interface, locally (i.e., slice maximum) at ≈73 s (SOC_{anode} ≈0.16) and globally (i.e., slice-averaged) at ≈109 s (SOC_{anode} ≈0.21) (cf, Fig. 7a). Significant electrolyte depletion starts at ≈61 s (SOC_{anode} ≈0.14) and eventually occurs for the back ≈60 μm of the graphite (cf, Fig. 7b). The electrolyte concentration profile within the anode is roughly flat for the first 2/3 of the anode, from the current collector side, indicating that electrolyte depletion, when it occurs, impacts a significant portion of the anode. Very high electrolyte concentrations are calculated at the back of the cathode (≈4 kmol.m^{-3}). However, for this range of concentration, the electrolyte properties are not well known. Especially, the diffusivity is assumed constant, ≈1e^{-11} m^2.s^{-1}, above 3.5 kmol.m^{-3} (cf, Fig. A5-1d), which can bias the results locally. Extrapolating the experimentally measured diffusivity would have resulted in near zero values (cf, Fig. A5-1d) and prevented numerical convergence. The graphite through-plane intercalation current density gradient is noticeable when electrolyte depletion occurs (≈61 s, SOC_{anode} ≈0.14). Eventually very high fluxes are predicted near the separator interface, ≈45 A.m^{-2}, that is

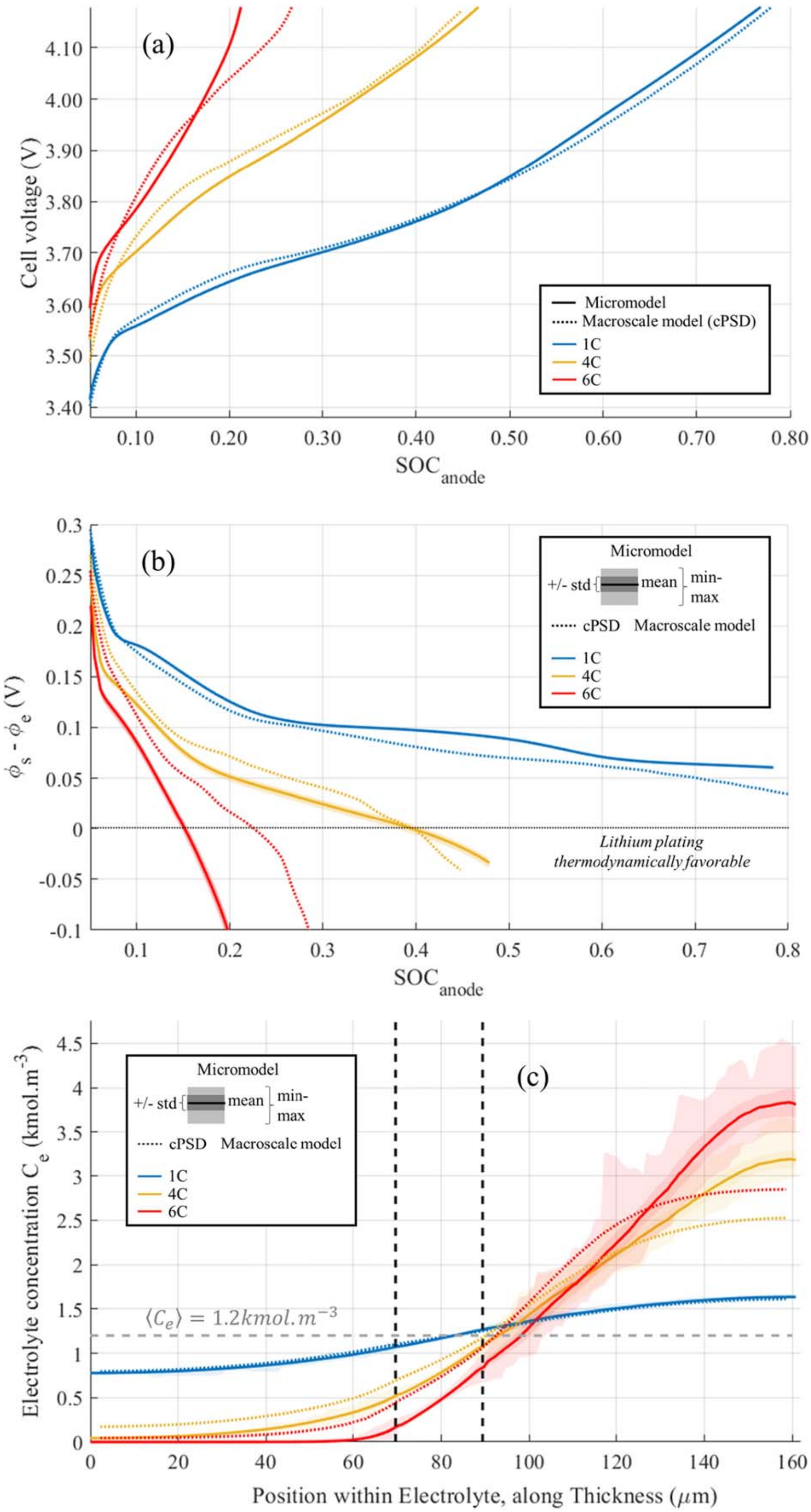

Figure 4. (a) Cell voltage, (b) potential for lithium plating, (c) electrolyte concentration through-plane profile at $\langle SOC_{anode} \rangle = 0.20$ calculated for round 2 cell with macroscale model (dashed lines) and microstructure scale model (solid lines).

$\approx$8.3 times higher than the volume-average. Such high local flux disproportionately stresses the particles near the separator. However, the current model does not consider chemo-mechanical stress and associated fracture degradation mechanisms. While a very high gradient is calculated at the front of the anode, the model predicts a near flat profile for the nearly 2/3 of the anode, near the current collector side. In comparison to the graphite, NMC intercalation current density through-plane gradient is significantly smaller

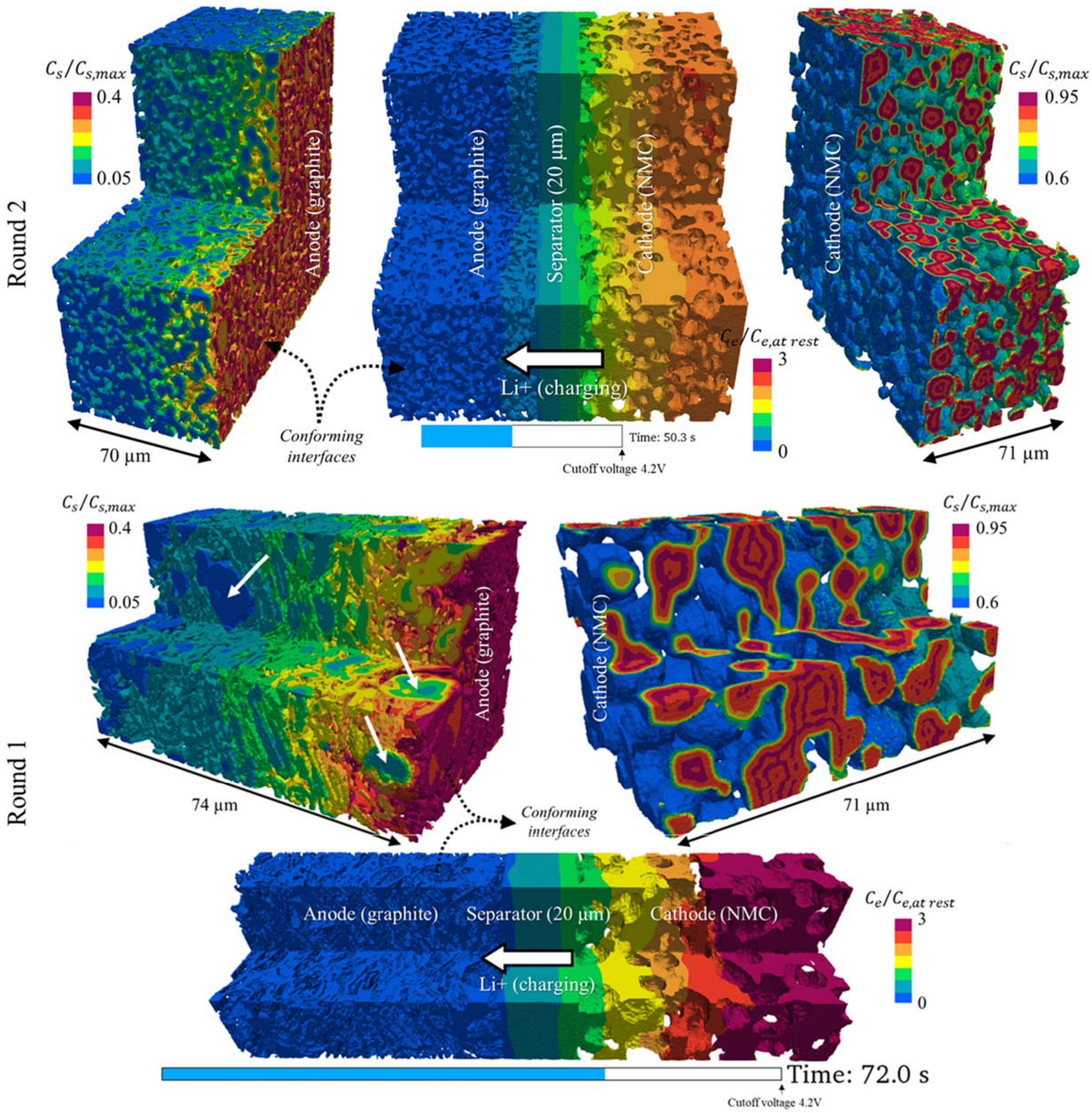

Figure 5. Concentration solution fields of (top) round 2 cell and (bottom) round 1 cell during 6 C charge. White line indicates large particles lagging behind the lithiation process for A12 graphite. Round 2 lithiation supplementary video is available online.

(cf, Fig. 7e). The most noticeable feature is the slope relaxation that leads to a flat profile at ≈73 s (SOC_{anode} ≈0.16). The intercalation current density in the graphite is not monotonic along the cell thickness, especially at low charge rate, with several slope inversions predicted by the model (cf, Fig. 9). The model demonstrated good numerical stability, being able to solve both electrolyte depletion and solid saturation (cf, Figs. 7a and 7b), due to the numerical features presented in Ref. 10 and due to the materials coefficients' wide validity range (cf, Fig. A5-1).

Figure 8 shows the through-plane electrolyte concentration profile calculated at different charge rates from 0.5 C to 6 C. Here, electrolyte depletion is not predicted to occur for C-rates below 4 C. In-plane electrolyte concentration heterogeneity for the C-rate investigated is located mostly at the back of the cathode and is increasing with C-rate. Figure 9 shows the graphite intercalation current density along the anode depth for a variety of C-rates and at different average SOC timestamps. The plots show a very dynamic through-plane profile at low-intermediate charge rate, with a flux (and a flux in-plane heterogeneity) propagation front from the anode-separator interface to the back of the electrode. That is the maximum current density is moving from the front (separator side) to the back (current collector side) of the anode while exhibiting ripples. As the front of the electrode is lithiating/saturating, and since there is no electrolyte depletion at the back of the anode for these low-intermediate charge rates, the intercalation current density progressively transitions toward the back of the anode. For high charge rates, the in-plane heterogeneity scales locally with the flux. For low-intermediate C-rate (⩽ ∼3 C), local high current does not always match with local high in-plane heterogeneity current. This indicates that the intrinsic mechanism that regulates the in-plane heterogeneity current is not just the current itself. This regulating mechanism is later discussed in Part II.[33]

Discussion

On the relevance of microscale model.—Lower scale models are not necessarily systemically more precise or relevant as compared with their higher scale counterpart models, especially considering

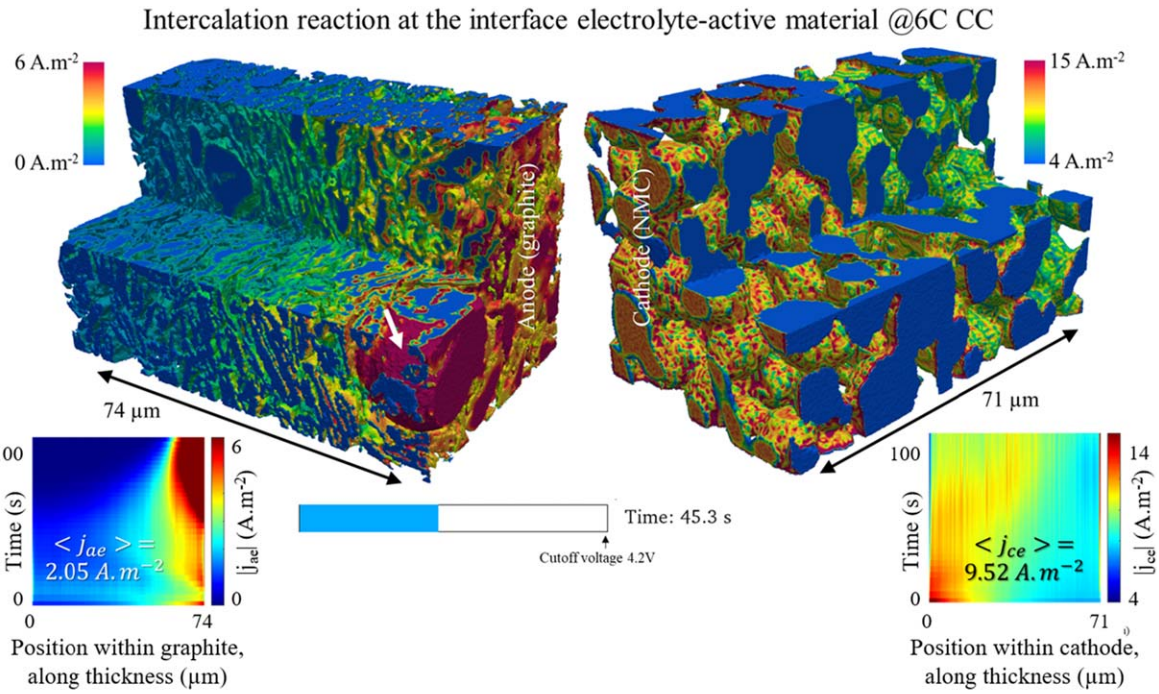

Figure 6. Faraday current density of round 1 cell. White line indicates large particles with significantly higher reaction flux compared with neighbored smaller particles. 2D maps show the evolution of the average intercalation current density in the anode (left) and the cathode (right).

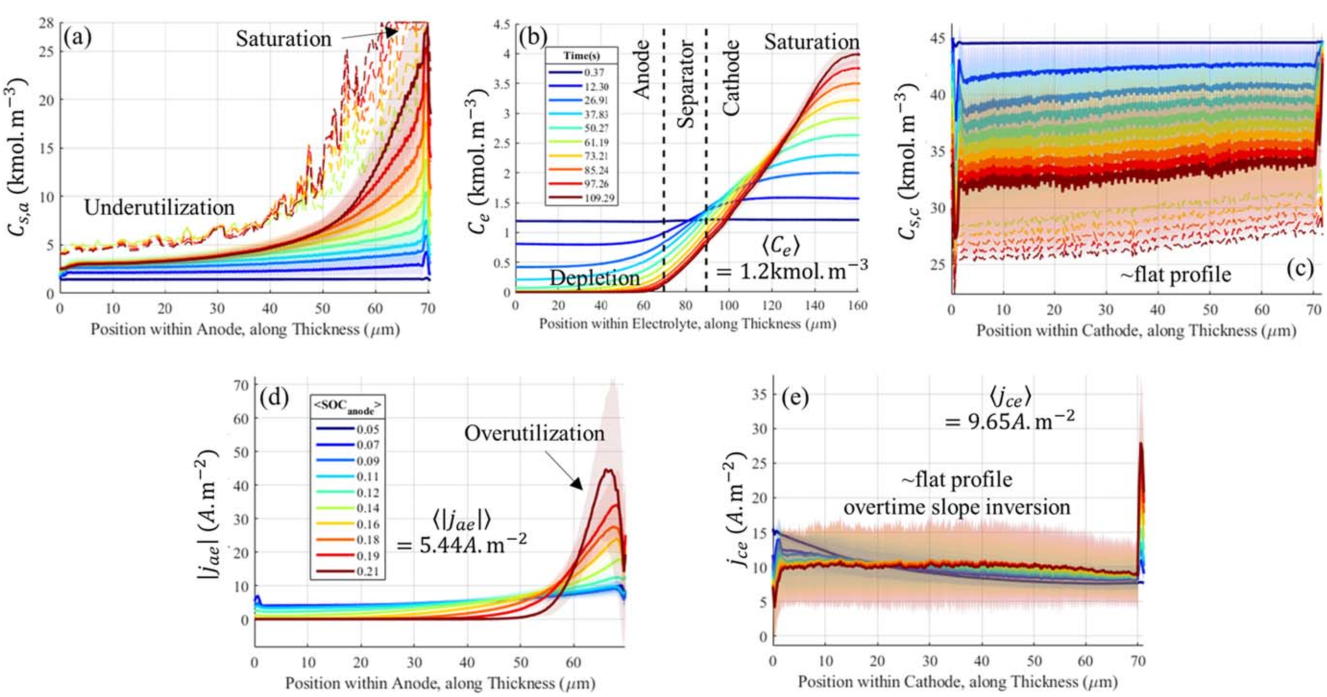

Figure 7. Through-plane heterogeneity within the round 2 cell during a 6 C CC charge. Concentration through-plane profiles for (a) anode, (b) electrolyte, (c) cathode. Intercalation current density through-plane profiles for (d) anode and (e) cathode. Solid line is slice-averaged concentration, transparent area is slice-standard deviation. Dashed lines, when present, are local (a) maximum or (c) minimum.

their higher computational cost.[10] The choice of the model scale depends on the electrode microstructures (scale and magnitude of the heterogeneity, particle morphology, microstructure evolution), material properties (transport and kinetics parameters), the scope of the analysis (performance-focused or degradation-focused), and the operating conditions (low or high temperature, slow or fast-charge). For instance, cases for which cells have relatively low microstructure heterogeneity, quasi-spherical particles, and are operated at a relatively low/intermediate charge rates (such that transport properties at the operating temperature are high enough to homogenize in-plane concentration and potential fields) are best simulated using a macroscale model. Deviations from these low-heterogeneity scenarios would eventually trigger deviations in the electrochemical cell behavior as predicted by a microscale model, but not for a macroscale model as there is not an explicit parameter that considers microstructure heterogeneity. This does not mean a macroscale

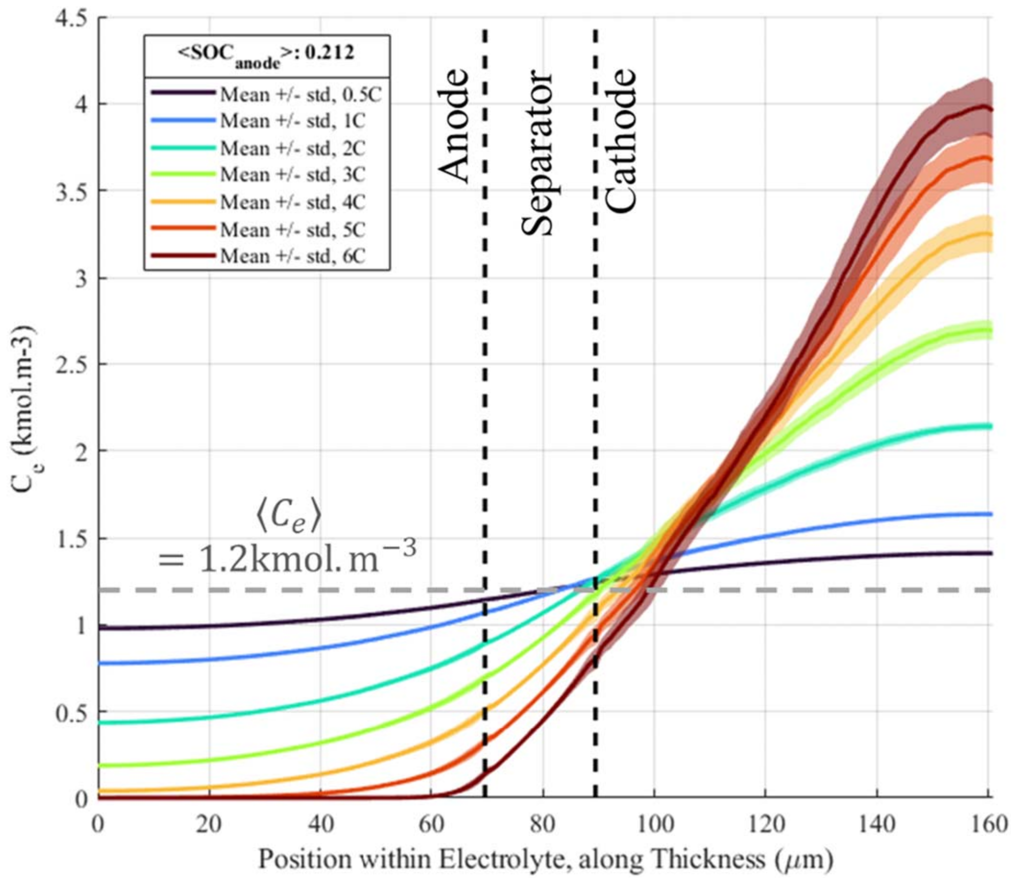

Figure 8. Round 2 cell through-plane electrolyte concentration profile at different charge rates. The curves are taken at different timestamps, but at same average graphite SOC. The solid line is the slice-averaged concentration, the transparent area is the standard deviation calculated per slice.

model cannot be used to predict high-heterogeneity scenarios, but to capture such effects will likely need to overfit some parameters (which may result in a new range of problems) to match experimental data, to accommodate for the partly inaccurate model assumptions. This emphasizes that the comparison analysis between micro- and macroscale models is essential, as micromodels can quantify the cost of heterogeneity on performance and degradation but can also be used eventually to identify the range of validity of widely used battery macroscale models and quantify the penalty of using incorrect higher-scale assumptions in these models. The "range of validity," in this context, means that both micro- and macroscale models are in agreement, given that (1) the same physics and same material properties are used, (2) the microstructure parameters are adequate (for the macroscale model), and (3) the microstructure is representative and finely detailed enough (for the microstructure scale model). The best choice, in this particular case, is considered to be the microscale model, as it requires less assumptions as compared to the macroscale model. Predicted differences between the microstructure model and the surrogate macroscopic model would imply one or several assumptions of the macroscale-model are incorrect (e.g., spherical particles) and that the operating conditions (e.g., high C-rate) highlight this incorrect assumption enough to influence the predicted polarization response. Eventually, thorough comparison studies could quantify these deviations over a wide range of conditions. In practice, such a deviation-mapping would substitute the implicit, potentially misleading, overfitting with new parameter(s) explicitly capturing microstructure heterogeneity effects. Previous work[2] established that there is a quantitative correlation between the tortuosity factor and the electrode porosity, particle morphology/alignment, and pore topology. However, in the previous work, only averaged properties were considered. Further work is required to relate tortuosity factor, or other effective parameters, with microstructure heterogeneity. The aim would be to explicitly capture the effect of the microstructure heterogeneity in macroscale models and be able to discriminate between different underlying microstructures with for instance poor particle alignment but high uniformity, and good particle alignment but poor uniformity. Quantitative correlation between microstructure heterogeneity and performance degradation could be then used to determine quality control constraints for battery manufacturers. Such microstructure heterogeneity can be quantified, for instance with a RVE size or a size-distribution variance. Numerically generated microstructures with controlled heterogeneities could be used to establish such correlations.

In this work, we were able to show larger differences between the two models for the real microstructure (high-heterogeneity case) as compared to the numerically generated microstructure (high uniformity case). However, a noticeable difference between the microstructure and macroscopic model remains even for the uniform case at high charge rates (similarly with Lopata et al.,[29]). This suggests that an intrinsic difference subsists between the geometry modeled between the macroscale and microscale models, despite both simulating spherical particles. Additional work is required to first nullify these differences between the microscale and macroscale models when there is no microscopic heterogeneity especially when operating at high charge rates. Two possible explanations are proposed to explain this discrepancy:

1. Particles are all connected due to the absence of the additive phase, which implies:

   - An additional lithium transport mode exists in the microscale model, as lithium can be exchanged directly between particles without passing through the electrolyte, while in the macroscale

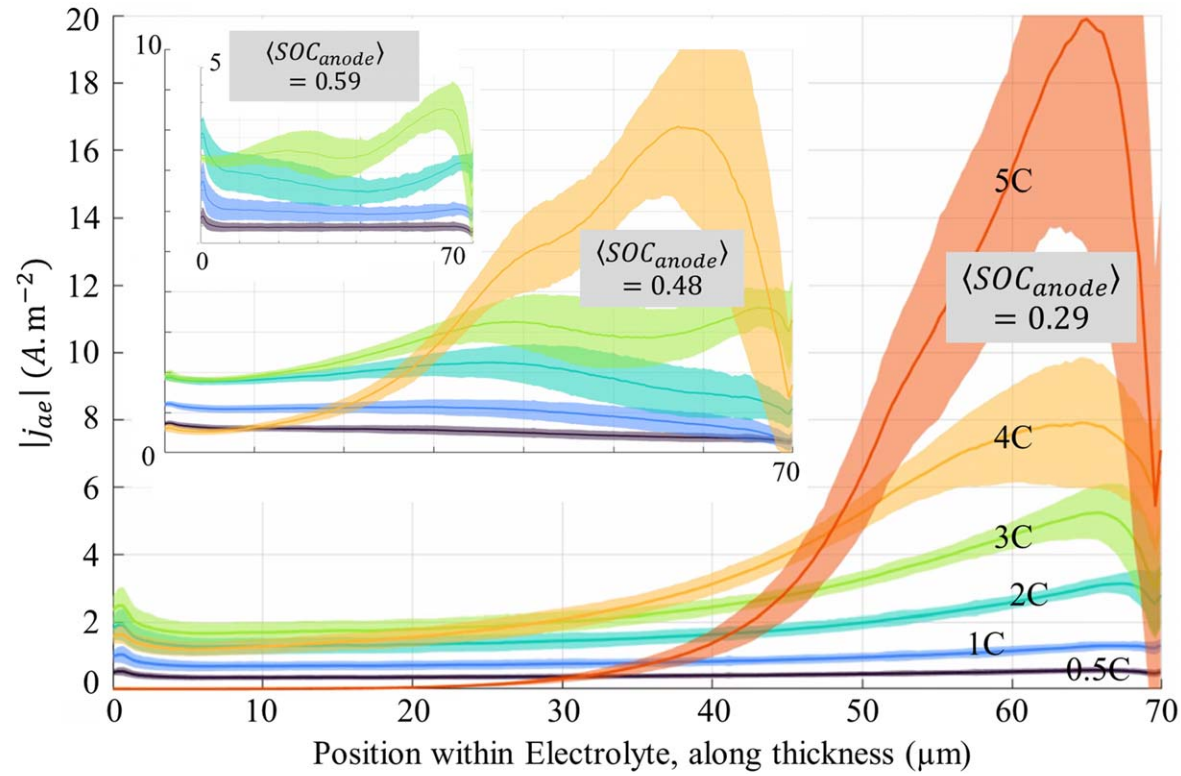

Figure 9. Round 2 cell through-plane graphite Faraday current density profile at different charge rate. Curves have been taken at 3 different average graphite SOC. Current scale (*y*-axis) is different for each graph. Solid line is slice-averaged current density, transparent area is slice-standard deviation. Supplementary video available online.

model redistribution of solid-phase lithium must be communicated between particles through the electrolyte. Such additional transport mode in the microscale model may lower the predicted polarization response.

- Non-radial (de)lithiation exists in the micromodel, as contacts between particles break the ideal geometry isotropy of a single isolated sphere. Furthermore, non-uniform curvature, typically at the junctions between connected particles, causes significant local concentration heterogeneities (as detailed in Part II[33]), which can then propagate to the extracted observable (e.g., voltage response).

2. Generating spatially randomly distributed particles does not guarantee some regions will not have slightly lower or higher porosities. While such local variations are averaged by definition in a macroscale model, they would induce local concentration and potential variations in a microscale model that could cause a shift in the average electrochemical behavior. Indeed, such local variations would not necessarily balance themselves as the rule of mixture does not apply due to both in-series and in-parallel interactions. Indeed, the rule of mixture (that is a volume-averaged effective transport properties) is only valid for volumes or materials spatially arranged in parallel along the transport direction and without transversal interactions between them.[57]

To remedy these issues, a micromodel should represent the active material complementary volume using a dual homogenization approach (effective electrolyte diffusivity *and* effective solid conductivity), which is beyond the current capability of the models discussed here. This capability would allow for non-overlapping spheres and thus completely enforce the uniformity and isotropy condition present in the macroscopic P2D model. Furthermore, to avoid local porosity variations, particles should be generated to be roughly equidistant (although without relying on a periodic pattern that would otherwise result in an oscillating porosity).

On the impact of tortuosity anisotropy and its consequence for macroscale modeling.—A particular interest is to quantify if tortuosity anisotropy negatively impacts the macroscale predictions, even though when the through-plane tortuosity factor (i.e., along the cell thickness) is accurately represented. Through-plane tortuosity factors are correlated with tortuosity factor anisotropy, both being related with the porosity and particle elongation (i.e., particle anisotropy induces *both* high through-plane tortuosity and through-plane tortuosity anisotropy for a given porosity), cf, Fig. 28 of previous work.[2] Therefore, the microstructure representation error in the macroscale model for cases *a* and *m* (respectively, aligned and misaligned ellipsoids, that is volumes with a non-zero tortuosity anisotropy) is likely due not to the absence of an in-plane or anisotropy tortuosity factor coefficient in the macroscale model. Say otherwise, when one is using a high tortuosity factor in a macroscale model, it implies (not necessarily but typically for battery electrodes microstructures) a non-zero tortuosity factor anisotropy (as the two are correlated[2]). That is, there is likely no need to add a coefficient that explicitly takes into account the tortuosity factor anisotropy to improve the model predictions. If macroscale model errors cannot be explained by the 1D description of the tortuosity, then the other limitations of the models, especially the spherical representation of the particles, are to blame. This suggests that electrodes with high tortuosity factors, typically induced by a combination of low porosity *and* particle morphology anisotropy, would be better modeled with a modified macroscale model with an additional radial dimension for the solid-state diffusion, i.e., a pseudo-3D model (1D thickness, + 2D long and short diameters), rather than with an additional in-plane dimension for the electrolyte transport. Such a P3D model would partly alleviate the microstructure oversimplification of the P2D model, which is especially relevant for capturing lithiation dynamics present in flake-like graphite electrodes, while avoiding the computational complexity of microscale model, offering a middle ground between complexity and fidelity.

Conclusions

On the hidden surface area parameter of microscale models.— It was implicitly considered that, given a FOV large enough, an image resolution high enough, and all phases visible, that the microstructure volume in a microscale model can completely substitute the macroscale set of microstructure parameter $\{\varepsilon, S_p, D_{50}, \tau\}$. However, the apparent fractal behavior of battery materials implies that the active interface area is not resolved. Using the surface area calculated at a given image resolution assumes the cut-off resolution is reached, beyond which the surface roughness disappears.[49] With literature suggesting a sub-nanometer or nanometer cut-off resolution,[49,58] well beyond the capabilities of current 3D imaging compatible with a large FOV, this means that the surface mesh is very likely not adequately resolved. The relevant image resolution for battery materials, regarding the active interface area, is yet unknown. This has a practical consequence on microscale modeling for real materials, as it implies modelers should explicitly set a specific surface area S_p, obtained either from experiment, fitting, or by assuming explicitly a given surface roughness. In this work, a surface roughness correction factor $S_{r,m}$ is used (cf, Table A4-II). Microstructure scale models then have a microstructure parameter set of size 2 (and not 1): {3D volume, S_p}. Note that surface smoothing, while providing visually appealing meshes and generally improving numerical convergence, does not resolve the issue. On the contrary, such mesh preprocessing aggravates the problem as smoothing actually reduces surface roughness and thus the surface area from a mesh for which it is believed surface roughness is already underestimated. Given the high uncertainty on the true specific surface area, it is suggested that $S_{r,m}$ is a prime candidate for fitting, before fitting other material parameters to avoid overfitting. This remark is also true for S_p in macroscale models.

On differences between predictions from micro- and macroscale models.— The microstructure scale model systematically predicts a significantly higher electrolyte concentration compared to the macroscale model at the back of the cathode near the current collector, with differences increasing with the C-rate, up to ∼330 and ∼1000 $mol.m^{-3}$ at 6 C, respectively, for numerically generated and real microstructures. Such discrepancy is concomitant with significant in-plane heterogeneity predicted by the microscale model on the same locations. This result suggests neglecting in-plane heterogeneities as done at the macroscale representation can affect averaged quantities. It is hypothesized local in-plane variations calculated in the microscale model in adjacent regions of the electrode volume do not balance out as, in a complex microstructure, pore regions are not ordained in parallel (that is transversal interactions exist) that prevent relying on a rule of mixture to homogenize the effective transport behavior. This has practical consequences, as due to mass conservation, predicting a higher electrolyte concentration at the back of the cathode aggravates electrolyte depletion at the back of the anode and thus exacerbates the anode material over-utilization near the separator.

Regarding the surface potential, the microscale model gets more conservative as the C-rate is increasing, eventually predicting the lithium plating onset at ≈0.15 SOC_{anode} as compared to ≈0.22 SOC_{anode} for the macroscale model at 6 C for the real microstructures. However, for the numerically generated microstructures, the macroscale model is slightly more conservative. Such difference could be the consequence of the real microstructures being much more heterogeneous than the numerically generated ones. Lithium plating heterogeneity and correlation with the electrode microstructure are further investigated in Part III[34] of this article series.

On material non-uniform utilization.— The microstructure scale model predicts significant non-uniform utilization along the cell thickness, as typically observed with macroscale models, namely solid concentration saturation at the front of the anode (i.e., near the separator) and electrolyte depletion at the back of the anode (i.e., near the current collector) at fast charge. The model also predicts a dynamic profile for the intercalation current density in the anode, especially at low and intermediate charge rates, with a reaction front moving from the separator to the back of the electrode as the overall lithiation progress. The microscale model predicts very heterogeneous three-dimensional concentration fields, that is, high in-plane concentration heterogeneity in addition to the gradation along the cell thickness, that are subsequently quantified and explained in Part II[33] of this article series.

Acknowledgments

Funding is provided by the U.S. DOE Office of Vehicle Technology Energy Storage Program, eXtreme Fast Charge and Cell Evaluation of Lithium-Ion Batteries (XCEL) Program, program manager Samuel Gillard. This work is authored by the National Renewable Energy Laboratory, United States, operated by Alliance for Sustainable Energy, LLC, for the U.S. Department of Energy (DOE) under Contract No. DE-AC36-08GO28308. A portion of the research was performed using computational resources sponsored by the Department of Energy's Office of Energy Efficiency and Renewable Energy and located at the National Renewable Energy Laboratory. The views expressed in the article do not necessarily represent the views of the DOE or the U.S. Government. The U.S. Government retains and the publisher, by accepting the article for publication, acknowledges that the U.S. Government retains a nonexclusive, paid-up, irrevocable, worldwide license to publish or reproduce the published form of this work, or allow others to do so, for U.S. Government purposes.

ORCID

Francois L. E. Usseglio-Viretta https://orcid.org/0000-0002-7559-8874
Andrew M. Colclasure https://orcid.org/0000-0002-9574-5106
Jeffery Allen https://orcid.org/0000-0003-2815-6835
Peter J. Weddle https://orcid.org/0000-0002-1600-0756
Donal P. Finegan https://orcid.org/0000-0003-4633-560X
Kandler Smith https://orcid.org/0000-0001-7011-0377

References

1. F. Usseglio-Viretta and K. Smith, *ECS Trans.*, **77**, 1095 (2017).
2. F. L. E. Usseglio-Viretta, D. P. Finegan, A. Colclasure, T. M. M. Heenan, D. Abraham, P. Shearing, and K. Smith, *J. Electrochem. Soc.*, **167**, 100513 (2020).
3. F. L. E. Usseglio-Viretta et al., *J. Electrochem. Soc.*, **165**, A3403 (2018).
4. A. M. Colclasure et al., *Electrochim. Acta*, **337**, 135854 (2020).
5. A. M. Colclasure, A. R. Dunlop, S. E. Trask, B. J. Polzin, A. N. Jansen, and K. Smith, *J. Electrochem. Soc.*, **166**, A1412 (2019).
6. M. Doyle and J. Newman, *Electrochim. Acta*, **40**, 2191 (1995).
7. K. Smith and C.-Y. Wang, *J. Power Sources*, **160**, 662 (2006).
8. A. Jokar, B. Rajabloo, M. Désilets, and M. Lacroix, *J. Power Sources*, **327**, 44 (2016).
9. W. Mai, A. Colclasure, and K. Smith, *J. Electrochem. Soc.*, **166**, A1330 (2019).
10. J. M. Allen, J. Chang, F. L. E. Usseglio-Viretta, P. Graf, and K. Smith, *J. Sci. Comput.*, **86**, 42 (2021).
11. P. Pietsch, M. Ebner, F. Marone, M. Stampanoni, and V. Wood, *Sustain Energy Fuels*, **2**, 598 (2018).
12. K. S. Mayilvahanan et al., *J. Electrochem. Soc.*, **168**, 070537 (2021).
13. D. P. Finegan et al., *Energ Environ Sci.*, **13**, 2570 (2020).
14. A. P. Monasterial et al., *Small Sci*, **3**, 2200067 (2023).
15. A. Mistry, K. Smith, and P. P. Mukherjee, *Acs Appl Mater Inter*, **12**, 16359 (2020).
16. A. Mistry, F. L. E. Usseglio-Viretta, A. Colclasure, K. Smith, and P. P. Mukherjee, *J. Electrochem. Soc.*, **167**, 090542 (2020).
17. M. M. Forouzan, B. A. Mazzeo, and D. R. Wheeler, *J. Electrochem. Soc.*, **165**, A2127 (2018).
18. W. Mai, F. L. E. Usseglio-Viretta, A. M. Colclasure, and K. Smith, *Electrochim. Acta*, **341**, 136013 (2020).
19. K. Higa, S.-L. Wu, D. Y. Parkinson, Y. Fu, S. Ferreira, V. Battaglia, and V. Srinivasan, *J. Electrochem. Soc.*, **164**, E3473 (2017).
20. B. Yan, C. Lim, L. Yin, and L. Zhu, *J. Electrochem. Soc.*, **159**, A1604 (2012).

21. T. Danner, M. Singh, S. Hein, J. Kaiser, H. Hahn, and A. Latz, *J. Power Sources*, **334**, 191 (2016).
22. A. H. Wiedemann, G. M. Goldin, S. A. Barnett, H. Zhu, and R. J. Kee, *Electrochim. Acta*, **88**, 580 (2013).
23. T. Hutzenlaub, S. Thiele, N. Paust, R. Spotnitz, R. Zengerle, and C. Walchshofer, *Electrochim. Acta*, **115**, 131 (2014).
24. A. Kashkooli, S. Farhad, D. U. Lee, K. Feng, S. Litster, S. K. Babu, L. Zhu, and Z. Chen, *J. Power Sources*, **307**, 496 (2016).
25. S. A. Roberts, H. Mendoza, V. E. Brunini, B. L. Trembacki, D. R. Noble, and A. M. Grillet, *Journal of Electrochemical Energy Conversion and Storage*, **13**, 031005 (2016).
26. X. Lu et al., *Nat. Commun.*, **11**, 2079 (2020).
27. R. Xu, Y. Yang, F. Yin, P. Liu, P. Cloetens, Y. Liu, F. Lin, and K. Zhao, *J. Mech. Phys. Solids*, **129**, 160 (2019).
28. P. Liu, R. Xu, Y. Liu, F. Lin, and K. Zhao, *J. Electrochem. Soc.*, **167**, 040527 (2020).
29. J. S. Lopata, T. R. Garrick, F. Wang, H. Zhang, Y. Zeng, and S. Shimpalee, *J. Electrochem. Soc.*, **170**, 020530 (2023).
30. H. Mendoza, S. A. Roberts, V. E. Brunini, and A. M. Grillet, *Electrochim. Acta*, **190**, 1 (2016).
31. A. Latz and J. Zausch, *Beilstein J Nanotech*, **6**, 987 (2015).
32. M. Meyer, L. Komsiyska, B. Lenz, and C. Agert, *Appl Math Model*, **37**, 2016 (2012).
33. F. L. E. Usseglio-Viretta, A. M. Colclasure, J. Allen, P. J. Weddle, D. P. Finegan, P. Graf, and K. Smith, *J. Electrochem. Soc.*, (PART II of this article series).
34. F. L. E. Usseglio-Viretta, A. M. Colclasure, J. Allen, P. J. Weddle, D. P. Finegan, P. Graf, and K. Smith, *J. Electrochem. Soc.*, (PART III of this article series).
35. L. Zielke, T. Hutzenlaub, D. R. Wheeler, C.-W. Chao, I. Manke, A. Hilger, N. Paust, R. Zengerle, and S. Thiele, *Adv. Energy Mater.*, **5**, 1401612 (2015).
36. M. Kroll, S. L. Karstens, M. Cronau, A. Höltzel, S. Schlabach, N. Nobel, C. Redenbach, B. Roling, and U. Tallarek, *Batter Supercaps*, **4**, 1363 (2021).
37. S. R. Daemi, C. Tan, T. Volkenandt, S. J. Cooper, A. Palacios-Padros, J. Cookson, D. J. L. Brett, and P. R. Shearing, *ACS Appl. Energy Mater.*, **1**, 3702 (2018).
38. F. L. E. Usseglio-Viretta et al., *J. Electrochem. Soc.*, **169**, 070519 (2022).
39. A. N. Mistry, K. Smith, and P. P. Mukherjee, *Acs Appl Mater Inter*, **10**, 6317 (2018).
40. B. L. Trembacki, D. R. Noble, V. E. Brunini, M. E. Ferraro, and S. A. Roberts, *J. Electrochem. Soc.*, **164**, E3613 (2017).
41. F. L. E. Usseglio-Viretta, P. Patel, E. Bernhardt, A. Mistry, P. P. Mukherjee, J. Allen, S. J. Cooper, J. Laurencin, and K. Smith, *SoftwareX*, **17**, 100915 (2022).
42. MATBOX: Microstructure Analysis Toolbox. NREL Transportation & Mobility Research, Data and Tools, https://www.nrel.gov/transportation/matbox.
43. F. L. E. Usseglio-Viretta, A. M. Colclasure, J. Allen, P. J. Weddle, D. P. Finegan, P. Graf, and K. Smith, *J. Electrochem. Soc.*, (PART IV of this article series).
44. T. Kanit, S. Forest, I. Galliet, V. Mounoury, and D. Jeulin, *Int. J. Solids Struct.*, **40**, 3647 (2003).
45. H. Xu, F. Usseglio-Viretta, S. Kench, S. J. Cooper, and D. P. Finegan, *J. Power Sources*, **480**, 229101 (2020).
46. M. J. Lacey, F. Jeschull, K. Edström, and D. Brandell, *J. Phys. Chem. C*, **118**, 25890 (2014).
47. A. Quinn, H. Moutinho, F. Usseglio-Viretta, A. Verma, K. Smith, M. Keyser, and D. P. Finegan, *Cell Reports Phys Sci*, **1**, 100137 (2020).
48. J. M. Allen et al., *J. Power Sources*, **512**, 230415 (2021).
49. A. Bertei, E. Ruiz-Trejoa, K. Kareh, V. Yufit, X. Wang, F. Tariq, and N. P. Brandona, *Nano Energy*, **38**, 526 (2017).
50. D. A. Rajon, P. W. Patton, A. P. Shah, C. J. Watchman, and W. E. Bolch, *Med. Phys.*, **29**, 682 (2002).
51. G.-H. Kim, K. Smith, J. Lawrence-Simon, and C. Yang, *J. Electrochem. Soc.*, **164**, A1076 (2017).
52. F. B. Planella et al., *Prog Energy*, **4**, 042003 (2022).
53. A. P. Tran, S. Yan, and Q. Fang, *Proc. SPIE*, **7**, 1 (2020).
54. Q. Fang and D. A. Boas, *2009 Ieee Int Symposium Biomed Imaging Nano Macro*, 1142 (2009).
55. F. Usseglio-Viretta, J. Laurencin, G. Delette, J. Villanova, P. Cloetens, and D. Leguillon, *J. Power Sources*, **256**, 394 (2014).
56. J. Joos, T. Carraro, M. Ender, B. Rüger, A. Weber, and E. Ivers-Tiffée, *ECS Trans.*, **35**, 2357 (2011).
57. J. Wang, J. K. Carson, M. F. North, and D. J. Cleland, *Int. J. Heat and Mass Transfer*, **49**, 3075 (2006).
58. S.-S. Liu, L. C. Saha, A. Iskandarov, T. Ishimoto, T. Yamamoto, Y. Umeno, S. Matsumura, and M. Koyama, *Commun. Chem.*, **2**, 48 (2019).